A thermosyphon-driven hydrothermal flow-through cell for *in situ* and time-resolved neutron diffraction studies

Fang Xia,[a,b,c] Brian O'Neill,[c] Yung Ngothai,[c] Jason Peak,[c] Christophe Tenailleau,[d] Barbara Etschmann,[a,b] Gujie Qian,[a,e] Joël Brugger,[a,b] Andrew Studer,[f] Scott Olsen[f] and Allan Pring[a,b]*

[a]Department of Mineralogy, South Australian Museum, North Terrace, Adelaide, SA 5000, Australia, [b]School of Earth and Environmental Sciences, University of Adelaide, North Terrace, Adelaide, SA 5005, Australia, [c]School of Chemical Engineering, University of Adelaide, North Terrace, Adelaide, SA 5005, Australia, [d]Laboratoire de Chimie des Matériaux Inorganiques et Energétiques, Université Paul Sabatier, Bâtiment 2R1, 118 Route de Narbonne, 31062 Toulouse Cedex, France, [e]Ian Wark Research Institute, University of South Australia, Mawson Lakes Campus, SA 5095, Australia, and [f]The Bragg Institute, Australian Nuclear Science and Technology Organization, PMB 1, Menai, NSW 2234, Australia. Correspondence e-mail: allan.pring@samuseum.sa.gov.au

A flow-through cell for hydrothermal phase transformation studies by *in situ* and time-resolved neutron diffraction has been designed and constructed. The cell has a large internal volume of 320 ml and can operate at temperatures up to 573 K under autogenous vapor pressures (*ca* 8.5 $\times$ 10^6 Pa). The fluid flow is driven by a thermosyphon, which is achieved by the proper design of temperature difference around the closed loop. The main body of the cell is made of stainless steel (316 type), but the sample compartment is constructed from non-scattering Ti–Zr alloy. The cell has been successfully commissioned on Australia's new high-intensity powder diffractometer WOMBAT at the Australian Nuclear Science and Technology Organization, using two simple phase transformation reactions from $KAlSi_2O_6$ (leucite) to $NaAlSi_2O_6{\cdot}H_2O$ (analcime) and then back from $NaAlSi_2O_6{\cdot}H_2O$ to $KAlSi_2O_6$ as examples. The demonstration proved that the cell is an excellent tool for probing hydrothermal crystallization. By collecting diffraction data every 5 min, it was clearly seen that $KAlSi_2O_6$ was progressively transformed to $NaAlSi_2O_6{\cdot}H_2O$ in a sodium chloride solution, and the produced $NaAlSi_2O_6{\cdot}H_2O$ was progressively transformed back to $KAlSi_2O_6$ in a potassium carbonate solution.

1. Introduction

Many chemical reactions occur under hydrothermal conditions (Shrivastava *et al.*, 1991). Notable examples include the nucleation, growth and phase transformations of crystalline solids (Kaneko *et al.*, 1983; Sczancoski *et al.*, 2009). Such reactions are responsible for ore formation and alteration processes in nearly all ore deposits, particularly so in the case of gold and base metal deposits (Robb, 2005). Hydrothermal reactions are also responsible for many ore processing and hydrothermal metallurgical processes (Venkatachalam, 1998), and are important routes for producing a wide range of inorganic technological materials, ranging from native elements to the most complex oxides, silicates, germanites, phosphates, carbonates, chalcogenides, titanates and tungstates (*e.g.* Nassau, 1980; Cheetham & Day, 1992; Byrappa & Yoshimura, 2001; Kolen'ko *et al.*, 2002; Zhang *et al.*, 2003; Xia *et al.*, 2008; Cavalcante *et al.*, 2009). A thorough understanding of the mechanisms of these hydrothermal reactions is thus of great importance to a wide range of fields in the earth, chemical and physical sciences. However, in spite of many studies, our knowledge of the mechanisms of these hydrothermal processes is still limited, especially with respect to reaction kinetics (Putnis, 2009; Tenailleau *et al.*, 2006; Xia *et al.*, 2007; Xia, Brugger, Chen *et al.*, 2009; Xia, Brugger, Ngothai *et al.*, 2009; Zhao *et al.*, 2009). One reason for this is the lack of efficient tools to study these processes *in situ*, as existing methods are largely limited to *ex situ* measurements; thus researchers can only elucidate the mechanisms and kinetics by characterizing quenched samples (Barnes, 1997; Byrappa & Yoshimura, 2001). The disadvantages of *ex situ* tools are that the solids may have undergone phase transitions or other unpredictable reactions during the cooling cycle; for some products, rapid redox reactions under ambient conditions may prevent their real nature being revealed; also, some reactions involve intermediates that are only stable at reaction

conditions and thus cannot be detected by *ex situ* techniques. An ideal approach to probe these hydrothermal processes is the use of *in situ* tools, by which the reactions can be directly observed and characterized under high-temperature and -pressure conditions, thus providing fuller understanding of the reaction mechanisms and the solution controls on them.

Most currently available techniques are not readily amenable to the study of hydrothermal reactions *in situ*, because such reactions are normally conducted in sealed and thick-walled cells, and usually under corrosive conditions. Fortunately, techniques utilizing electromagnetic radiation or neutron waves are able to provide *in situ* information using specially designed hydrothermal cells because they can couple and penetrate certain materials. For example, many researchers have explored *in situ* hydrothermal reactions using techniques including UV–vis spectroscopy (Kawamura, 2002), Raman spectroscopy (Hurst *et al.*, 2002; Maslar *et al.*, 2009), IR spectroscopy (Kieke *et al.*, 1996; Kazarian & Martirosyan, 2002), X-ray absorption spectroscopy (Brugger *et al.*, 2007; Liu *et al.*, 2007), angular dispersive X-ray diffraction (ADXRD) (Norby, 1997; Webster *et al.*, 2009), energy dispersive X-ray diffraction (EDXRD) (Evans *et al.*, 1995; Francis *et al.*, 1999; Jorgensen *et al.*, 2008), neutron diffraction (ND) (Walton *et al.*, 1999; O'Neill *et al.*, 2006), small-angle X-ray scattering (Testemale *et al.*, 2005), small-angle neutron scattering (Dokter *et al.*, 1994) and nuclear magnetic resonance (Gerardin *et al.*, 2000).

Among these techniques, the powder diffraction techniques (ADXRD, EDXRD and ND) have unique advantages for reactions involving the evolution of crystalline solids, because these solids are readily detected by diffraction and the method is amenable to fully quantitative phase analysis. Furthermore, recent increases in flux in synchrotron X-ray radiation and neutron sources enable quality diffraction patterns to be collected very rapidly, making time-resolved investigations possible. This is particularly important to extract kinetic data for reactions that occur over a few hours or less.

To date the major obstacle limiting the use of the *in situ* diffraction techniques has been the general scarcity of suitable hydrothermal cells that can operate at elevated temperatures and pressures. For ADXRD, two capillary cells were developed at Brookhaven National Laboratory (Norby, 1997; Norby, Cahill *et al.*, 1998), and were used in the study of hydrothermal zeolite crystallization up to *ca* 523 K (Norby, Poshni *et al.*, 1998). The disadvantage of these capillary cells is that one can only study a tiny volume of sample (<2 µl), which, given that processes such as crystal nucleation are volume dependent, may give kinetic data that are not representative of the reactions at laboratory or industrial scale. Very recently Webster *et al.* (2009) developed a flow cell for the Australian Synchrotron. This cell has a volume of ∼0.1 ml and is suitable for studying scale formation under Bayer processing conditions. However, the cell uses a 20 µm-thick Melinex window, which restricts its use to low temperatures (up to *ca* 343 K). For EDXRD, Evans and co-workers developed a laboratory-scale cell (25 ml) that was successfully used to study the hydrothermal syntheses of microporous materials (Francis *et al.*, 1999) and sulfide growth (Cahill *et al.*, 2000), and can operate at up to *ca* 523 K. The cell body was made of steel and thus the intensity of the diffraction patterns was greatly attenuated owing to the absorption of the beam by the cell wall. This problem was somewhat ameliorated in a later design by using an aluminium cell (Engelke *et al.*, 2003), but the lower tensile strength of aluminium restricts the operation to low pressures (the cell was operated at up to *ca* 443 K under autogeneous vapor pressure). For ND, Walton *et al.* (1999) constructed a 23 ml cell that was employed in the study of the mechanisms of hydrothermal syntheses of materials (Walton *et al.*, 2001; Williams *et al.*, 2006). This cell uses a magnetic bar for stirring, which limits its application to temperatures below the Curie point of the magnetic material (*ca* 423 K).

Recently, our group initiated the design and construction of large volume (>200 ml) flow-through cells for studying phase transformations by *in situ* neutron diffraction (O'Neill *et al.*, 2006). The large volume is essential to keep the fluid composition relatively unchanged so that the mechanism and kinetics can be studied under tightly constrained solution chemistry (Carlson, 2002). This simplifies the data interpretation because hydrothermal reactions are usually complex and a significant change of fluid composition during the course of the reaction can change the mechanism drastically (Xia, Brugger, Chen *et al.*, 2009; Zhao *et al.*, 2009). The fluid flow is particularly important for mineral phase transformation studies because it mimics natural formation conditions within the Earth's crust. The first prototype flow-through cell had an internal volume of 280 ml (O'Neill *et al.*, 2006) and was used to study the transformation of pentlandite $(Fe,Ni)_9S_8$ to violarite $(Fe,Ni)_3S_4$. However, the fluid flow was controlled by a magnetic micro-pump, which restricts its use to temperatures below the Curie point (*ca* 423 K) of the magnetic elements.

Here we describe a novel larger-volume (320 ml) flow-through cell capable of working at higher temperatures (up to 573 K) for *in situ* neutron diffraction experiments, employing a thermosyphon to drive the fluid circulation. The commissioning of the cell was performed on Australia's new high-intensity powder diffraction neutron beamline WOMBAT at the Australian Nuclear Science and Technology Organization (ANSTO) using two model transformation reactions, $KAlSi_2O_6$ (leucite) to $NaAlSi_2O_6{\cdot}H_2O$ (analcime) and then back from $NaAlSi_2O_6{\cdot}H_2O$ to $KAlSi_2O_6$, to prove the utility of the cell design for *in situ* study of phase transformations under hydrothermal conditions.

2. Cell design

2.1. Basic design

The aim of the design is twofold. First, we want to achieve a relatively large fluid volume (>200 ml) whilst simultaneously retaining a high signal-to-noise ratio during neutron diffraction experiments. Second, we desire that the cell be able to work at higher temperatures (> 423 K), thereby avoiding the limitation of the micro-pump-driven cell (O'Neill *et al.*, 2006). To achieve the first aim, the key consideration is the central

component of the cell, the sample compartment. On one hand, the sample compartment needs to be large enough to hold a few grams of solid sample, because compared to X-ray sources, neutron interaction is weaker and neutron beams have a larger size. On the other hand, the sample compartment also needs to be sufficiently slim to reduce the attenuation of the beam due the moderating effects of deuterated fluids. Also, in order to dampen changes in fluid chemistry during the transformation or reaction a relatively large volume of fluid is required, but to reach high temperatures (>423 K) a magnetic micro-pump cannot be used. A balance of these criteria means that the sample compartment volume must be limited to several millilitres, but a large volume of fluid must move through the sample compartment during the reaction.

To achieve these design features we employed a flow-through circulation loop (Fig. 1), by which we are able to keep the sample compartment as small as possible and at the same time have a large volume of fluid circulating around the rest of the loop. The fluid circulation is achieved by employing the thermosyphon principle, which works more efficiently at higher temperatures (> *ca* 393 K). The design allows the cell to operate at temperatures up to *ca* 573 K, but this value could be increased easily by utilizing components with higher tensile strengths. An over pressure of gas, up to 1.0×10^7 Pa, can also be used, employing a gas regulator connected to the top of the loop. The modification to the cell design is straightforward as a modular construction has been employed using mainly standard commercial (Swagelok) components (http://www.swagelok.com). In the following, we will describe the details of individual components.

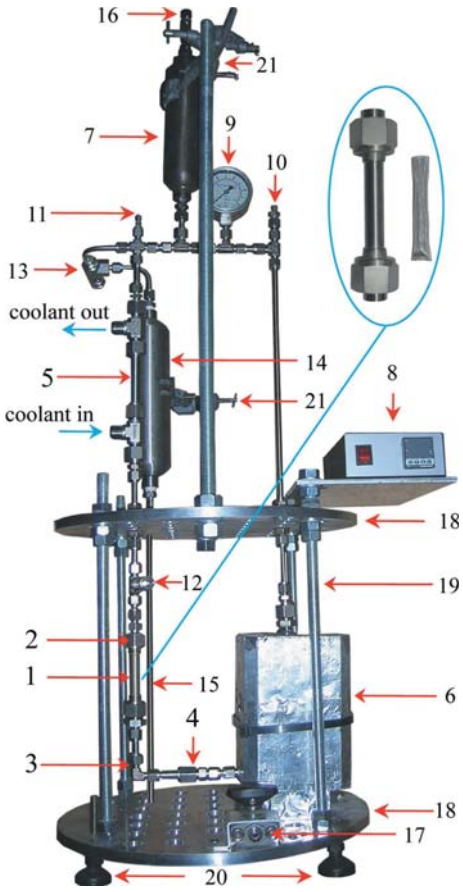

Figure 1
The flow-through hydrothermal cell. (1) Ti–Zr alloy sample compartment (an enlarged view as well as the stainless steel basket are shown in the inset); (2) reducing union; (3) elbow; (4) metal gasket face-seal fitting; (5) heat exchanger; (6) ceramic blocks, wrapping the tabular heater and the fluid reservoir; (7) expansion vessel; (8) temperature controller; (9) pressure gauge; (10) thermocouple insertion point (for fluid reservoir); (11) thermocouple insertion point (for heat exchanger); (12) thermocouple insertion point (for sample compartment); (13) pressure relief valve; (14) buffer vessel; (15) condensation tube; (16) top valve; (17) bottom fill/drain ball valve; (18) supporting plates; (19) threaded supporting rods; (20) height-adjustable feet; (21) clamps. The surveillance camera and the plastic filling pipe are not shown; the aluminium shield and the bottom spill tray are shown in Fig. 2.

2.2. Thermosyphon loop

The thermosyphon is designed to ensure efficient fluid circulation around the loop to damp out changes in solution chemistry during any transformation or reaction. The thermosyphon loop is rectangular in shape, 600 mm high and 165 mm wide, and has an internal volume of 320 ml. The loop consists of a 150 ml fluid reservoir (Swagelok, 316 L-50DF4-150) wrapped by a mini tubular heater (590 W, HELIOS; Item 6, Fig. 1), a temperature controller (Shinko JCR-33A-S/M; Item 8, Fig. 1) that precisely controls the heater, a 150 ml expansion vessel (Swagelok, 316 L-HDF4-150) for fluid expansion at elevated temperatures (Item 7, Fig. 1), a 180 mm double-pipe cooling heat exchanger (constructed from Swagelok fittings; Item 5, Fig. 1), a sample compartment (Item 1, Fig. 1), and $\frac{1}{4}''$ (6.35 mm) tubing and a series of Swagelok connectors and fittings. All the Swagelok fittings and tubing are stainless steel (316 type). The fluid reservoir and the heater are wrapped by two ceramic insulation blocks to minimize heat loss. The fluid in the reservoir is heated, becoming less dense, and as a consequence it rises up the tube. On the other side of the loop, the double-pipe heat exchanger removes the heat from the fluid using a cooling medium (generally compressed air). The cooling increases the density of the fluid, causing it to fall through the sample compartment by gravity and return to the fluid reservoir, where it is reheated and circulation continues. In this manner, both heating and cooling induce the fluid circulation. The temperatures at the center of the fluid reservoir, at the heat exchanger and in the sample compartment are monitored by three K-type thermocouples. The temperature difference between the heating and cooling points can be controlled by adjusting the flow rate of coolant through the heat exchanger, and hence the flow velocity v (m s^{-1}) can be adjusted according to the equation

$$v = \left\{ \frac{[\rho(T_0) - \rho(T)]\, gD}{3[\rho(T_0) + \rho(T)]\, f} \right\}^{1/2}, \qquad (1)$$

where ρ is the density (kg m^{-3}), T_0 and T are the temperatures (K) at the cooling and heating points, g is the acceleration of gravity (m s^{-2}), D is the internal diameter of the tube (m), and f is the friction factor between the fluid and the internal

surface of the tube. Typically, flow velocities from 0.03 to 0.21 m s^{-1} can be achieved in the temperature range from 393 to 573 K.

2.3. Sample compartment

The sample compartment is primarily composed of an open-ended tube connected to two Swagelok reducing unions (S-810-64) at each end (Items 2, Fig. 1). To reduce the absorption and scattering from the sample compartment, the tube is constructed from a zero-scattering Ti–Zr alloy (67.7 at.% Ti, 32.3 at.% Zr; New Metals and Chemicals Ltd, Waltham Abbey, UK), which has a zero average neutron scattering length, thereby giving no Bragg peaks in the diffraction patterns. The alloy also has excellent mechanical strength, which allows the cell to work at high pressures. The tube is 100 mm long, having an internal diameter of 9.5 mm and a wall thickness of 1.6 mm at the ends. The wall thickness of the middle part (45 mm long, neutron beam path) of the tube has been machined to 0.4 mm to reduce neutron absorption. The volume of the tube in the beam path is approximately 3 ml, and the tube is capable of holding a few grams of sample. To improve the corrosion resistance under hydrothermal conditions, the internal surface of the tube was electroplated first with a nickel and then with a gold layer. The nickel layer is used to enable the gold to bond on the Ti–Zr alloy.

The sample grains are wrapped into a cylinder-shaped 316 stainless steel fine-mesh basket with a diameter slightly larger than the internal diameter of the Ti–Zr tube, so that by slight folding the sample basket can be readily positioned at the middle of the vertically mounted sample compartment by the frictional force between the basket and the internal surface of the tube. With this basket, the fluid can flow through easily and, at the same time, the sample can be held firmly without being displaced from the beam center by the fluid flow. For easy sample exchange during a series of experiments, the bottom reducing union is connected to a Swagelok $\frac{1}{4}''$ metal gasket face-seal fitting with the aid of an elbow (Swagelok S-400-2; Items 3 and 4, Fig. 1).

2.4. Safety components

The cell performs at elevated temperatures and pressures with a large fluid volume, and at the center of an extremely expensive neutron diffraction instrument. Therefore, it is very important to minimize the risk of leakage from the cell or catastrophic failure of the mechanical components. The pressure is the dominant risk factor, so in the design we utilized a safety factor of two after carefully calculating the ultimate tensile strength of the constructing materials to ensure the cell operates safely at the most hostile working conditions (573 K and 8.5×10^6 Pa). Rigorous laboratory hydrostatic pressure tests were completed before the commissioning experiments at a pressure of 1.2×10^7 Pa corresponding to *ca* 1.4 times the maximum working pressure. No leakage was observed over a 72 h test period. In spite of the careful engineering, there is still the possibility of failure brought on by pressure overshoot as a result of, for example, temperature-controller failure, thermocouple failure, or even overfilling of the initial fluid by careless (or inexperienced) operators. To avoid pressure overshoot, a threefold-redundant safety system was implemented. (i) A pressure gauge (0–25 MPa, Swagelok; Item 9, Fig. 1) is fitted for pressure monitoring, and a surveillance camera is also installed for remote monitoring of the pressure gauge in the control room as a first measure. (ii) The more important measure is the inclusion of a pressure-relief valve (Swagelok, S-4R3A; Item 13, Fig. 1). This relief valve can be adjusted to a preset threshold pressure (in the case of the testing experiments it was set to 9.0×10^6 Pa); when the system pressure exceeds this threshold, the valve automatically opens to relieve the pressure by releasing part of the hydrothermal fluid/vapor until the system pressure returns to the threshold value. The fluid/vapor first goes through a 300 ml buffer vessel (Swagelok, 316 L-HDF4-300; Item 14, Fig. 1) and then a long condensation tube (Item 15, Fig. 1) and is finally collected by a large stainless steel spill tray at the bottom of the system, capable of containing the total volume of fluid. In the commissioning at ANSTO, we used another pressure-relief valve (Austral–Powerflo Solutions Type 3990) whose threshold pressure was set to 7.0×10^6 Pa. (iii) In addition to the pressure-relief system the cell is encased by a cylindrical aluminium shield, providing protection in case of catastrophic rupture due to failure of the pressure-relief system. The thickness of the shield is 1 mm, sufficient to intercept any fragments and debris without penetration, whilst not significantly attenuating the primary or scattered neutron beams. The diameter of the shield (340 mm) is less than that of the bottom spill tray (500 mm), so that the sprayed hydrothermal fluid can be captured by the internal surface of the shield and then drained into the spill tray. However, during laboratory tests lasting *ca* 5000 h (accumulated, each run for *ca* 20–200 h) no such catastrophic rupture was encountered. The worst situation that occurred was leaking caused by a loose connection, proving that the cell is very safe to operate.

2.5. Support platform

The loop is firmly positioned with the help of a support platform constructed mainly from aluminium. This platform is composed of two parallel 340 mm-diameter and 10 mm-thick plates (Item 18 Fig. 1), linked by five 300 mm-long threaded support rods (Item 19, Fig. 1), four adjustable feet (Item 20, Fig. 1) at the bottom to allow for setting the correct height in the neutron beam, and two pairs of clamps (Item 21, Fig. 1) for holding the expansion vessel and relief buffer vessel. The support plates contain 45 holes of 20 mm diameter to allow air influx and subsequent efficient thermal convection of the air around the cell, to aid with the operation of the thermosyphon at lower temperatures (<453 K). To avoid significant heat loss as a consequence of thermal conduction through the plates, hard vulcanized red fiber sealing washers are placed at the intersection between the loop and the plates to provide thermal resistance. For operation in excess of 473 K, insulating

glass fiber tape is wrapped around the loop, but not around the heat exchanger or the sample compartment.

2.6. Fill/drain system

The system is filled from the bottom of the cell employing the communicating vessel principle. This avoids the waste of costly deuterated fluids and the trapping of air pockets if filling from the top. Trapped air pockets can cause considerable temperature instability during experiments and would induce two-phase flow in the cell. To perform the filling, one end of a 1.2 m thin transparent plastic pipe (internal diameter 4 mm) is connected to the bottom fill/drain ball valve (Swagelok, S-33PS4; Item 17, Fig. 1), and the other end is connected to a plastic funnel. During filling, the funnel is held at a level higher than the valve on the top of the expansion tank (Item 16, Fig. 1), and the fluid is added slowly and continuously until the required volume is reached and the fluid level in the pipe does not change. With this method, a maximum of *ca* 8 ml of fluid may be wasted (in the plastic pipe), if not recycled. The total fluid volume in the cell is calculated to account for the internal expansion of the fluid when heated, ensuring that the system still has sufficient space in the expansion vessel under hydrothermal conditions.

The cell is drained by opening both the top and bottom valves, and by connecting the bottom valve to a collecting container using a plastic pipe. After draining, the system is rinsed with Milli-Q water by filling and draining the cell and then dried by flushing with compressed air for a few minutes from the top valve. This practice minimizes the contamination of the system between experimental runs.

3. Commissioning

To illustrate the capability of the new cell, the transformation reaction from $KAlSi_2O_6$ to $NaAlSi_2O_6{\cdot}H_2O$ and the reverse reaction from $NaAlSi_2O_6{\cdot}H_2O$ to $KAlSi_2O_6$ were studied at the new-generation Australian high-intensity constant-wavelength neutron powder diffractometer WOMBAT at ANSTO.

3.1. Setup of the instrument

The setup of the flow-through cell on WOMBAT is shown in Fig. 2. The neutron beam was directed *via* a thermal guide (TG1) from the OPAL reactor to the WOMBAT beamline where the wavelength ($\lambda \simeq 1.54$ Å) of the beam was selected using a 300 mm-high vertically focusing germanium (115) monochromator at a takeoff angle of 90° (Studer *et al.*, 2006). The beam size was shaped by a slit system and in this study the size was 20 mm (width) × 50 mm (height) so as to completely immerse the central part of the sample compartment in the beam. After impinging on the sample, the scattered neutrons first travelled through an oscillating radial collimator where unwanted parasitic Bragg scattering signals were eliminated. Then the remaining neutrons (diffraction signal) were detected by a 200 mm-high 120° position-sensitive area detector (15–135° in 2θ). The distance from the sample to the detector was 728 mm, providing ample space for the hydrothermal cell. The zero shift and the neutron wavelength were calibrated using an alumina (Al_2O_3) standard, and the intensities of the diffraction patterns were calibrated with an empty vanadium can.

The cell was placed on the sample stage with the sample compartment aligned at the beam center. The stainless steel reducing unions at both ends of the Ti–Zr sample compartment were wrapped with cadmium sheets to prevent possible diffraction signals from these joints. The thermocouple in the sample compartment was connected *via* a temperature-recording unit (LakeShore Model 340 Temperature Controller) to a computer in the control room to record the temperature profile during the experiments. The temperature of the heating reservoir was set to the target value, the neutron beam turned on and the data collection started.

The high neutron flux allowed the collection of high-quality data with adequate counting statistics in a relatively short time. As this study involved fluid phases, which significantly increased the background, we collected diffraction data every 5 min to balance the time resolution and signal-to-noise ratio.

3.2. Materials and methods

The leucite ($KAlSi_2O_6$) samples are natural crystals from a volcanic area near Rome, Italy. They were hand-selected, ultrasonically cleaned, crushed and sieved to grains with sizes ranging from 63 to 90 µm. Analytical grade NaCl ($\geq$99.5%) and K_2CO_3 ($\geq$99%) were ordered from Sigma–Aldrich. Heavy water (D_2O) was provided by ANSTO.

The phase quantification was performed using the Rietveld (1969) method with the aid of the computer program *GSAS* (Larson & Von Dreele, 2004; Toby, 2001). In each Rietveld least-square fitting, structure models were obtained from the Inorganic Crystal Structure Database [Nos. 9826 for $KAlSi_2O_6$, 2930 for $NaAlSi_2O_6{\cdot}H_2O$ and 103559 for stainless steel (Fe,Ni)]. The final qualified fitting gave mass fractions of involved phases, and the reaction extent y was then calculated by a general formula:

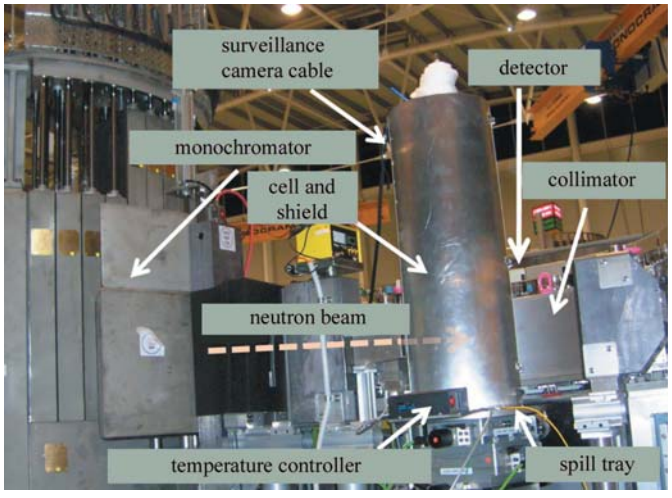

Figure 2
Setup of the flow-through cell on WOMBAT, the high-intensity powder diffractometer at ANSTO.

$$y = [(Y_0 - Y_t)/(Y_0 - Y_e)]100\%$$
$$= [(Y_0 - Y_t)/Y_0]100\% \quad (Y_e = 0), \qquad (2)$$

where Y_t, Y_0 and Y_e are the mass fractions of the reactant crystals at an arbitrary reaction time t, initially ($t = 0$) and at equilibrium ($t = \infty$), respectively. The kinetics were modeled by the empirical Avrami equation (Etschmann *et al.*, 2004):

$$\ln\ln[1/(1 - y)] = n \ln k + n \ln t. \qquad (3)$$

Then the rate constants k and the reaction-mechanism-dependent time exponent n were extracted by plotting $\ln\ln[1/(1 - y)]$ *versus* $\ln t$.

3.3. Initial tests

Initial tests were performed prior to hydrothermal phase transformation. First, patterns of the empty cell, the cell with sample basket and $KAlSi_2O_6$ (1 g), and the cell with sample basket, $KAlSi_2O_6$ (2 g) and reaction fluid (0.6 *M* NaCl) were recorded (Fig. 3). The reaction fluid was prepared with heavy water to avoid a high background from incoherent scattering of hydrogen from ordinary water. As expected, neither the non-scattering Ti–Zr empty cell nor the thin coating on the internal surface of the sample compartment give any Bragg peaks, resulting in an excellent flat background (Fig. 3*a*). After sample loading, Bragg peaks of $KAlSi_2O_6$ and the stainless steel basket were immediately seen (Fig. 3*b*). The addition of the reaction fluid increased the background, particularly at low 2θ (below 40°; Fig. 3*c*), where the $KAlSi_2O_6$ and $NaAlSi_2O_6{\cdot}H_2O$ diffraction peaks overlapped significantly with a broad peak from D_2O. This broad peak means that we must rely on diffraction data for $2\theta > 40°$ to follow the course of the reaction (Fig. 3*c*).

Diffraction patterns with the sample basket and reaction fluid were also collected at four temperatures (298, 463, 483 and 503 K; Fig. 4*a*). These patterns show five distinct peaks from the stainless steel basket, at around 43.78 (111), 50.92 (200), 74.77 (220), 90.75 (311) and 96.05° (222), which can serve as an internal standard in the phase transformation study. These Bragg peaks shift to lower angles with increasing temperature, reflecting the thermal expansion of the stainless steel (Fig. 4*b*). The linear thermal expansion coefficient was calculated to be 16.7 (14) $\times 10^{-6}$ K^{-1}, in good agreement with the value in the literature (17.7×10^{-6} K^{-1}; Dean, 1999). We also observed the variation of peak shape as well as the intensity of the broad D_2O peak with increasing temperature, which are probably due to the effect of the flow rate and/or the variation of scattering length of deuteron as a function of temperature.

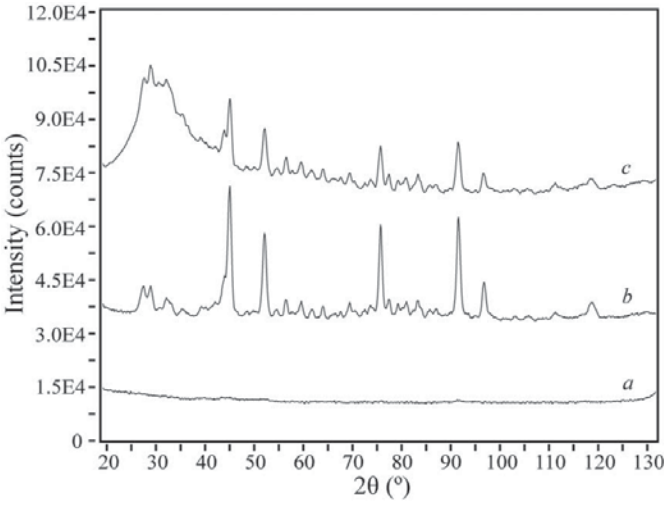

Figure 3
Diffraction patterns of (*a*) the empty Ti–Zr alloy sample compartment, showing no diffraction peaks, (*b*) $KAlSi_2O_6$ (1 g) in the stainless steel basket without solution (298 K) and (*c*) $KAlSi_2O_6$ (2 g) in the stainless steel basket in 0.6 *M* NaCl solution with D_2O as the solvent (363 K). Patterns *b* and *c* have been offset for a clearer comparison.

3.4. The transformations between $KAlSi_2O_6$ and $NaAlSi_2O_6{\cdot}H_2O$

The transformations between $KAlSi_2O_6$ and $NaAlSi_2O_6{\cdot}H_2O$ were used to demonstrate the practicality of the cell. The

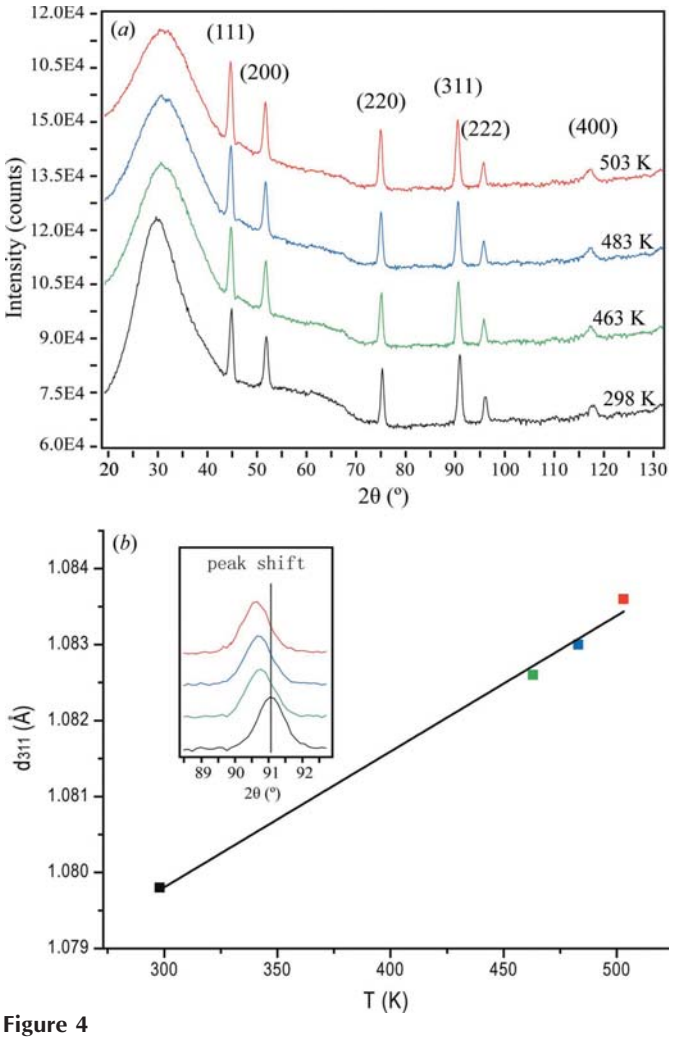

Figure 4
(*a*) Neutron diffraction patterns of the stainless steel basket at four temperatures in 0.6 *M* NaCl solution with D_2O as the solvent. (*b*) An enlargement of the (311) peak shift and the *d*-spacing linear fit. The *d* spacing was calculated by the commercial program *JADE* (http://www.materialsdata.com).

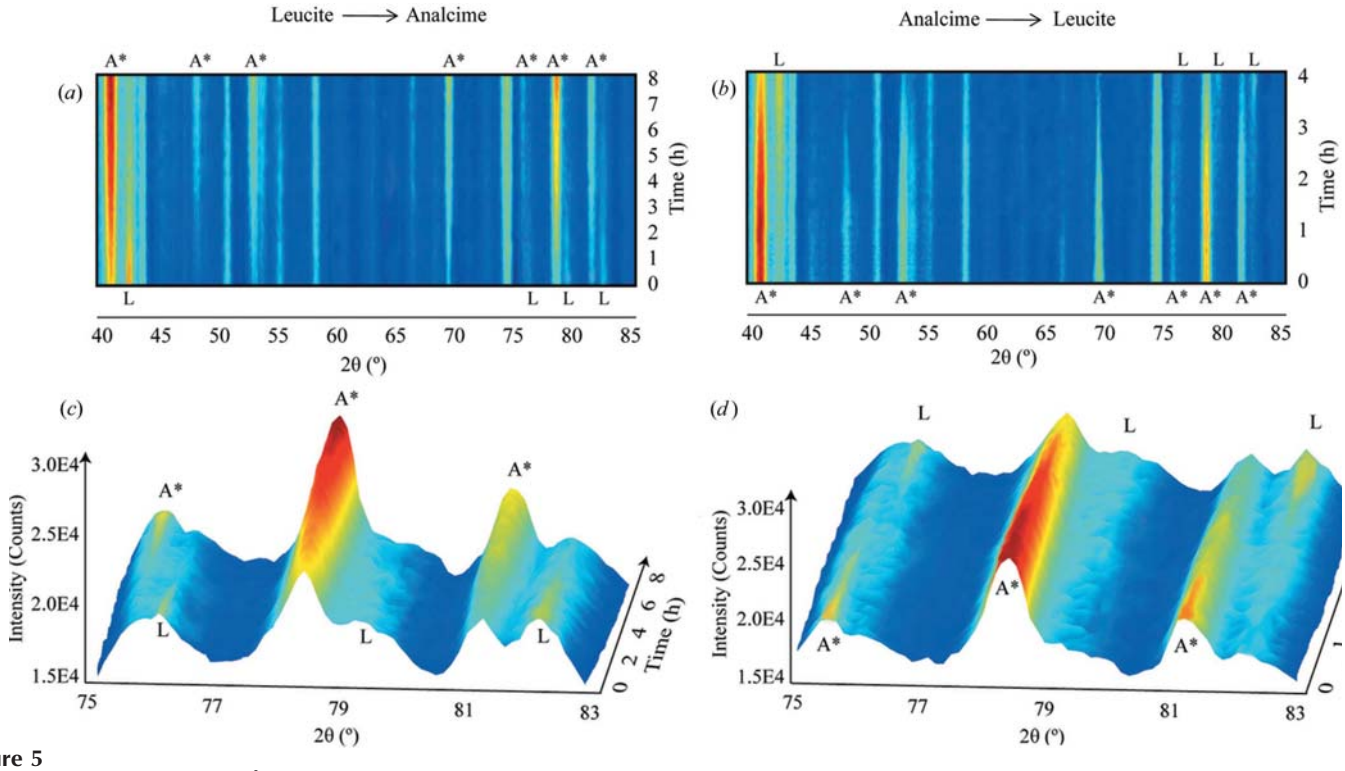

Figure 5
Neutron diffraction ($\lambda \simeq 1.54$ Å) patterns of the transformation (*a*), (*c*) from $KAlSi_2O_6$ to $NaAlSi_2O_6{\cdot}H_2O$ and (*b*), (*d*) from $NaAlSi_2O_6{\cdot}H_2O$ to $KAlSi_2O_6$. Background (D_2O plus stainless steel basket) has been subtracted to highlight the $KAlSi_2O_6$ and $NaAlSi_2O_6{\cdot}H_2O$ peaks. (*a*) and (*b*) are overviews of the reaction progress, and (*c*) and (*d*) are highlights of a small region. L = $KAlSi_2O_6$ peaks, A* = overlapped peaks where $NaAlSi_2O_6{\cdot}H_2O$ is the dominant phase.

transformation from $KAlSi_2O_6$ to $NaAlSi_2O_6{\cdot}H_2O$ is important in the weathering of some volcanic rocks and in the devitrification of some glasses (Karlsson & Clayton, 1991; Mazzi & Galli, 1978), and has been recently applied in the rational syntheses of nanozeolites (Xia, Brugger, Ngothai *et al.*, 2009). The two minerals have similar crystal structures ($KAlSi_2O_6$, tetragonal, space group $I4_1/a$ with $a = 13.041$, $c = 13.743$ Å; and $NaAlSi_2O_6{\cdot}H_2O$, cubic, space group $Ia\bar{3}d$ with $a = 13.723$ Å), allowing topotactic replacement to occur by the epitaxial nucleation of $NaAlSi_2O_6{\cdot}H_2O$ onto the $KAlSi_2O_6$ crystal lattice. This reaction has recently been confirmed to proceed *via* a coupled dissolution–reprecipitation replacement reaction mechanism (Putnis *et al.*, 2007), rather than (as traditionally believed) *via* solid-state cation exchange (Barrer & Falconer, 1956). The overall reaction can be written as

$$KAlSi_2O_6 + Na^+ + H_2O \rightarrow NaAlSi_2O_6{\cdot}H_2O + K^+. \quad (4)$$

The transformation from $NaAlSi_2O_6{\cdot}H_2O$ to $KAlSi_2O_6$ is also an important reaction in the alteration of engineered barrier components in contact with K^+-rich hyperalkaline fluids, as this reaction may affect the long-term performance of the barrier components. However, only a few studies have been devoted to the understanding of its mechanisms (Savage *et al.*, 2001). The overall reaction can be written as follows:

$$NaAlSi_2O_6{\cdot}H_2O + K^+ \rightarrow KAlSi_2O_6 + Na^+ + H_2O. \quad (5)$$

Previous studies were all based on *ex situ* techniques, by which possible intermediate phases during the reaction cannot be confirmed. Our *in situ* observations provide direct evidence of the phase evolution during reaction conditions.

The transformation from $KAlSi_2O_6$ to $NaAlSi_2O_6{\cdot}H_2O$ was performed at 503 K by reacting 2 g of $KAlSi_2O_6$, of a grain fraction of 53–90 µm, with 200 ml of 0.6 *M* NaCl solution. The progressive transformation is observed from the diffraction patterns (Figs. 5*a* and 5*c*). Phase quantifications were carried out using *GSAS*. A typical least-squares fitting of the partially transformed sample is shown in Fig. 6. The quantitative reaction progress is shown in Fig. 7. It is seen that in 8 h of reaction time ~80% of $KAlSi_2O_6$ was converted to NaAl-

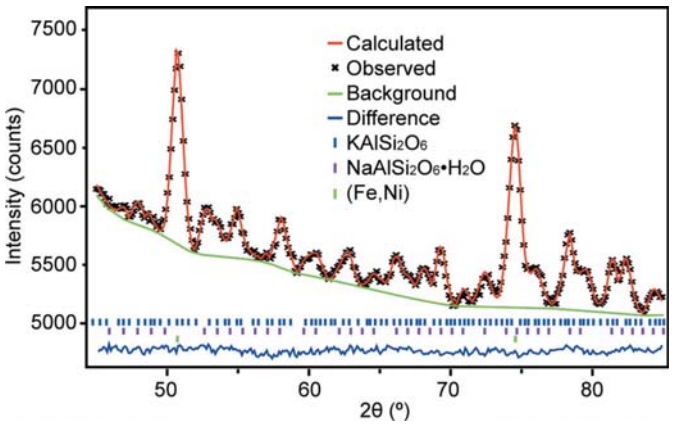

Figure 6
An example of phase quantification by Rietveld least-squares fitting using the *GSAS* program.

$Si_2O_6{\cdot}H_2O$. It is clear that $KAlSi_2O_6$ was directly transformed to $NaAlSi_2O_6{\cdot}H_2O$ as no intermediate phase was detected. The value of the Avrami rate constant k and the time component n are 4.36 (27) $\times$ 10^{-5} s^{-1} and 2.09 (1), respectively.

The transformation from $NaAlSi_2O_6{\cdot}H_2O$ to $KAlSi_2O_6$ was also performed at 503 K by reacting partially transformed $KAlSi_2O_6$ with 200 ml of 0.3 *M* K_2CO_3 solution. The progressive transformation is also shown in the diffraction patterns (Figs. 5*b* and 5*d*). The quantitative reaction progress is shown in Fig. 8. It is clear that ~70% of $NaAlSi_2O_6{\cdot}H_2O$ was converted back to $KAlSi_2O_6$ in 4 h without any intermediate phase. The value of the Avrami rate constant k and the time component n are 7.71 (62) $\times$ 10^{-5} s^{-1} and 1.95 (2), respectively. Note that the values of n for the two transformations are very close and also similar to other hydrothermal phase transformations [*e.g.* pentlandite to violarite (Xia, Brugger, Chen *et al.*, 2009)], implying that similar mechanisms dominate hydrothermal phase transformations.

Therefore, the phase transformations between $KAlSi_2O_6$ and $NaAlSi_2O_6{\cdot}H_2O$ are quite rapid at 503 K and there was no intermediate phase observed during *in situ* neutron diffraction.

4. Conclusions

We have designed, constructed and commissioned a large-volume hydrothermal flow-through cell for high-temperature *in situ* and real-time neutron diffraction studies, and demonstrated its ability to perform *in situ* measurements of hydrothermal chemical reactions involving crystalline solids. We used the simple phase transformations between $KAlSi_2O_6$ and $NaAlSi_2O_6{\cdot}H_2O$ as examples on the WOMBAT instrument at

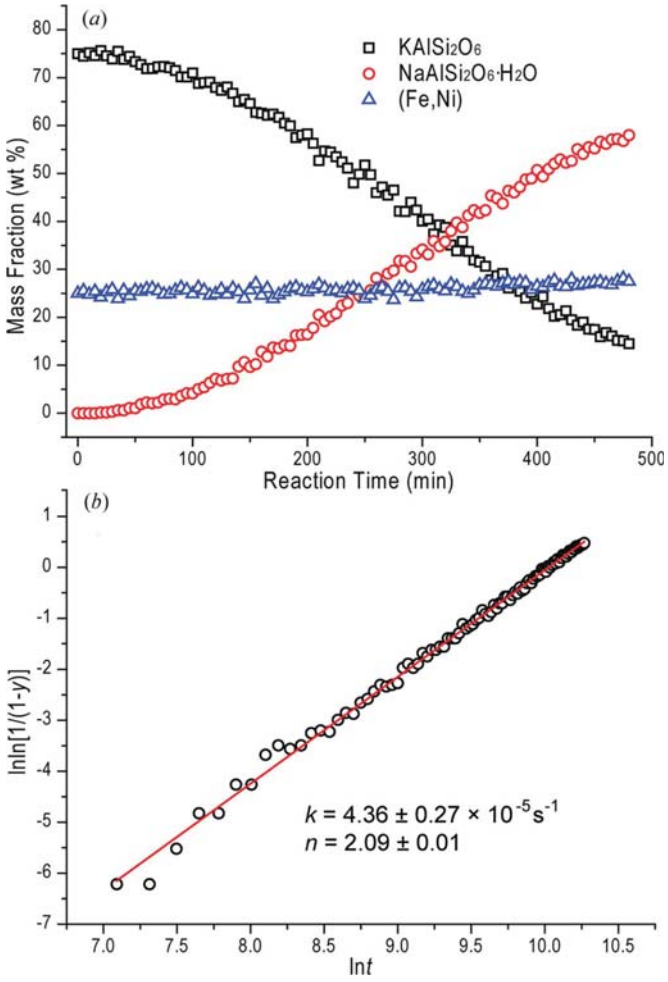

Figure 7
(*a*) Mass fractions of the three involved phases as a function of reaction time during the transformation from $KAlSi_2O_6$ to $NaAlSi_2O_6{\cdot}H_2O$. Note that the total mass of the sample changed from 2.00 g at the beginning of the reaction to 1.73 g at the end because of the loss of small particles from the mesh tube; however, the mass of the stainless steel mesh tube remained constant at 0.66 g, so the mass fraction of (Fe,Ni) slightly increased during the process, serving as an excellent internal standard for quantification. (*b*) An Avrami plot yields the rate constant k [4.36 (27) $\times$ 10^{-5} s^{-1}] and the time component n [2.09 (1)].

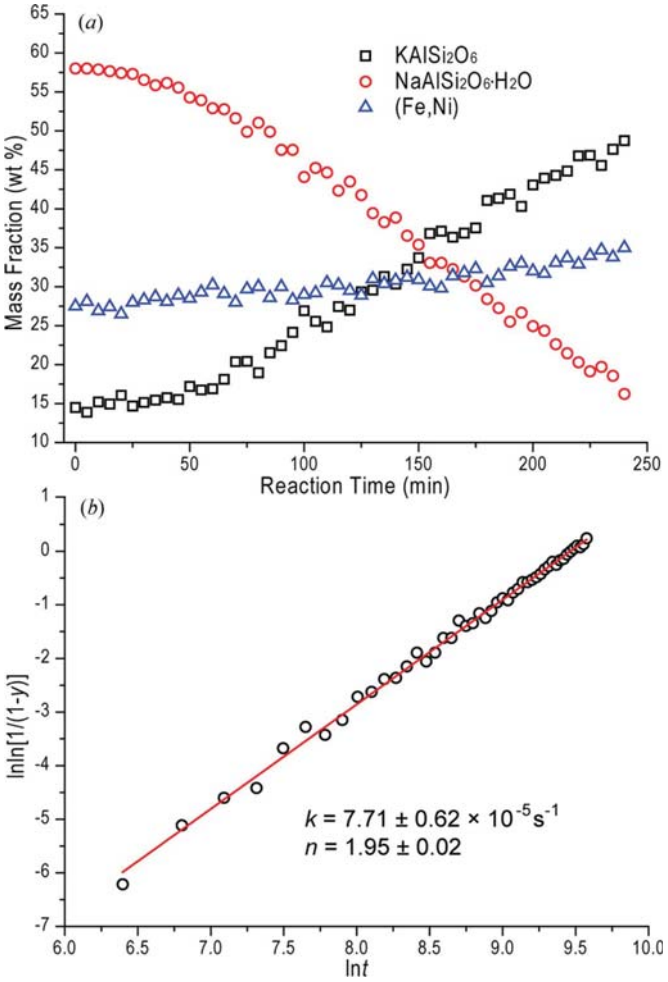

Figure 8
(*a*) Mass fractions of the three involved phases as a function of reaction time during the transformation from $NaAlSi_2O_6{\cdot}H_2O$ to $KAlSi_2O_6$. Note that the total mass of the sample changed from 1.73 g at the beginning of the reaction to 1.24 g at the end because of the loss of small particles from the mesh tube; however, the mass of the stainless steel mesh tube remained constant at 0.66 g, so the mass fraction of (Fe,Ni) slightly increased during the process, serving as an excellent internal standard for quantification. (*b*) An Avrami plot yields the rate constant k [7.71 (62) $\times$ 10^{-5} s^{-1}) and the time component n [1.95 (2)].

ANSTO, and showed that kinetic information on hydrothermal crystallization can be obtained easily with high time resolution. We expect this new tool to help in the study of more complex hydrothermal reactions, whose mechanisms and kinetics are still unknown or contentious. Applications to other important mineralogical phase transformations have been planned in the near future. Further improvements to the cell are possible: for example, use of a non-scattering Ti–Zr alloy basket to avoid Bragg peaks from the stainless steel basket. The construction of new cells based on similar design but customized for a particular situation has also been planned; for example, a cell suitable for studies under strongly acidic conditions is being built by replacing stainless steel with titanium. The current cell has been placed in ANSTO and is available to users from all over the world.

Thanks are due to ANSTO workshop for the improvements to the hydrothermal cell. The authors are grateful to Professor Gernot Kostorz and two anonymous reviewers for their valuable comments. This work was financially supported by the Australian Research Council (projects DP0344134 and DP0772299) and the Australian Institute of Nuclear Science and Engineering.

References

Barnes, H. L. (1997). Editor. *Geochemistry of Hydrothermal Ore Deposits*, 3rd ed. New York: John Wiley and Sons Inc.

Barrer, R. M. & Falconer, J. D. (1956). *Proc. R. Soc. London Ser. A*, **236**, 227–249.

Brugger, J., Etschmann, B., Liu, W., Testemale, D., Hazemann, J. L., Emerich, H., van Beek, W. & Proux, O. (2007). *Geochim. Cosmochim. Acta*, **71**, 4920–4941.

Byrappa, K. & Yoshimura, M. (2001). *Handbook of Hydrothermal Technology: A Technology for Crystal Growth and Materials Processing.* Norwich: Noyes Publications/William Andrew Publishing LLC.

Cahill, C. L., Benning, L. G., Barnes, H. L. & Parise, J. B. (2000). *Chem. Geol.* **167**, 53–63.

Carlson, W. D. (2002). *Am. Mineral.* **87**, 185–204.

Cavalcante, L. S., Sczancoski, J. C., Lima, L. F., Espinosa, J. W. M., Pizani, P. S., Varela, J. A. & Longo, E. (2009). *Cryst. Growth Des.* **9**, 1002–1012.

Cheetham, A. K. & Day, P. (1992). Editors. *Solid State Chemistry: Compounds.* Oxford: Clarendon Press.

Dean, J. A. (1999). *Lange's Handbook of Chemistry*, 15th ed. New York: McGraw-Hill Professional.

Dokter, W. H., Beelen, T. P. M., Vangarderen, H. F., Rummens, C. P. J., Vansanten, R. A. & Ramsay, J. D. F. (1994). *Colloids Surf. A*, **85**, 89–95.

Engelke, L., Schaefer, M., Porsch, F. & Bensch, W. (2003). *Eur. J. Inorg. Chem.* pp. 506–513.

Etschmann, B., Pring, A., Putnis, A., Grguric, B. A. & Studer, A. (2004). *Am. Mineral.* **89**, 39–50.

Evans, J. S. O., Francis, R. J., O'Hare, D., Price, S. J., Clark, S. M., Flaherty, J., Gordon, J., Nield, A. & Tang, C. C. (1995). *Rev. Sci. Instrum.* **66**, 2242–2245.

Francis, R. J., O'Brien, S., Fogg, A. M., Halasyamani, P. S., O'Hare, D., Loiseau, T. & Ferey, G. (1999). *J. Am. Chem. Soc.* **121**, 1002–1015.

Gerardin, C., Haouas, M., Lorentz, F. & Taulelle, F. (2000). *Magn. Reson. Chem.* **38**, 429–435.

Hurst, W. S., Hodes, M. S., Bowers, W. J., Bean, V. E., Maslar, J. E., Griffith, P. & Smith, K. A. (2002). *J. Supercrit. Fluids*, **22**, 157–166.

Jorgensen, J. E., Jensen, T. R. & Hanson, J. C. (2008). *J. Solid State Chem.* **181**, 1925–1929.

Kaneko, S., Aoki, H., Nonaka, I., Imoto, F. & Matsumoto, K. (1983). *J. Electrochem. Soc.* **130**, 2487–2489.

Karlsson, H. R. & Clayton, R. N. (1991). *Am. Mineral.* **76**, 189–199.

Kawamura, K. (2002). *Anal. Sci.* **18**, 715–716.

Kazarian, S. G. & Martirosyan, G. G. (2002). *Phys. Chem. Chem. Phys.* **4**, 3759–3763.

Kieke, M. L., Schoppelrei, J. W. & Brill, T. B. (1996). *J. Phys. Chem.* **100**, 7455–7462.

Kolen'ko, Y. V., Burukhin, A. A., Churagulov, B. R., Oleinikov, N. N. & Vanetsev, A. S. (2002). *Inorg. Mater.* **38**, 252–255.

Larson, A. C. & Von Dreele, R. B. (2004). Report LAUR 86-748. Los Alamos National Laboratory, New Mexico, USA.

Liu, W. H., Etschmann, B., Foran, G., Shelley, M. & Brugger, J. (2007). *Am. Mineral.* **92**, 761–770.

Maslar, J. E., Hurst, W. S., Bowers, W. J., Hendricks, J. H. & Windsor, E. S. (2009). *J. Electrochem. Soc.* **156**, C103–C113.

Mazzi, F. & Galli, E. (1978). *Am. Mineral.* **63**, 448–460.

Nassau, K. (1980). *Gems Made by Man.* Santa Monica: Gemological Institute of America.

Norby, P. (1997). *J. Am. Chem. Soc.* **119**, 5215–5221.

Norby, P., Cahill, C., Koleda, C. & Parise, J. B. (1998). *J. Appl. Cryst.* **31**, 481–483.

Norby, P., Poshni, F. I., Gualtieri, A. F., Hanson, J. C. & Grey, C. P. (1998). *J. Phys. Chem. B*, **102**, 839–856.

O'Neill, B., Tenailleau, C., Ngothai, Y., Struder, A., Brugger, J. & Pring, A. (2006). *Physica B*, **385–386**, 942–945.

Putnis, A. (2009). *Rev. Mineral. Geochem.* **70**, 87–124.

Putnis, C. V., Geisler, T., Schmid-Beurmann, P., Stephan, T. & Giampaolo, C. (2007). *Am. Mineral.* **92**, 19–26.

Rietveld, H. M. (1969). *J. Appl. Cryst.* **2**, 65–71.

Robb, L. (2005). *Introduction to Ore-Forming Processes.* Malden: Blackwell Science Ltd.

Savage, D., Rochelle, C., Moore, Y., Milodowski, A., Bateman, K., Bailey, D. & Mihara, M. (2001). *Mineral. Mag.* **65**, 571–587.

Sczancoski, J. C., Bomio, M. D. R., Cavalcante, L. S., Joya, M. R., Pizani, P. S., Varela, J. A., Longo, E., Li, M. S. & Andrés, J. A. (2009). *J. Phys. Chem. C*, **113**, 5812–5822.

Shrivastava, O. P., Komarneni, S. & Malla, P. (1991). *Mater. Res. Bull.* **26**, 357–366.

Studer, A. J., Hagen, M. E. & Noakes, T. J. (2006). *Physica B*, **385–386**, 1013–1015.

Tenailleau, C., Pring, A., Etschmann, B., Brugger, J., Grguric, B. A. & Putnis, A. (2006). *Am. Mineral.* **91**, 706–709.

Testemale, D., Coulet, M. V., Hazemann, J. L., Simon, J. P., Bley, F., Geaymond, O. & Argoud, R. (2005). *J. Chem. Phys.* **122**, 194505.

Toby, B. H. (2001). *J. Appl. Cryst.* **34**, 210–213.

Venkatachalam, S. (1998). *Hydrometallurgy.* New Delhi: Narosa.

Walton, R. I., Francis, R. J., Halasyamani, P. S., O'Hare, D., Smith, R. I., Performed, R. & Humphreys, R. J. (1999). *Rev. Sci. Instrum.* **70**, 3391–3396.

Walton, R. I., Millange, F., Smith, R. I., Hansen, T. C. & O'Hare, D. (2001). *J. Am. Chem. Soc.* **123**, 12547–12555.

Webster, N. A. S., Madsen, I. C., Loan, M. J., Scarlett, N. V. Y. & Wallwork, K. S. (2009). *Rev. Sci. Instrum.* **80**, 084102.

Williams, G. R., Norquist, A. J. & O'Hare, D. (2006). *Chem. Mater.* **18**, 3801–3807.

Xia, F., Brugger, J., Chen, G., Ngothai, Y., O'Neill, B., Putnis, A. & Pring, A. (2009). *Geochim. Cosmochim. Acta*, **73**, 1945–1969.

Xia, F., Brugger, J., Ngothai, Y., O'Neill, B., Chen, G. & Pring, A. (2009). *Cryst. Growth Des.* **9**, 4902–4906.

Xia, F., Zhou, J., Brugger, J., Ngothai, Y., O'Neill, B., Chen, G. & Pring, A. (2008). *Chem. Mater.* **20**, 2809–2817.

Xia, F., Zhou, J., Pring, A., Ngothai, Y., O'Neill, B., Brugger, J., Chen, G. & Colby, C. (2007). *React. Kinet. Catal. Lett.* **92**, 257–266.

Zhang, M.-S., Yu, J., Chu, J., Chen, Q. & Chen, W. (2003). *J. Mater. Process. Technol.* **137**, 78–81.

Zhao, J., Brugger, J., Grundler, P. V., Xia, F., Chen, G. & Pring, A. (2009). *Am. Mineral.* **94**, 1541–1555.